DC-Link Harmonics of Three-Phase Voltage-Source Converters Influenced by the Pulsewidth-Modulation Strategy—An Analysis

Michael H. Bierhoff and Friedrich Wilhelm Fuchs, *Senior Member, IEEE*

***Abstract*—DC-link current harmonics are the predominant factor to be considered for dimensioning dc capacitors in three-phase pulsewidth-modulation (PWM) voltage-source converters. In this paper, an analysis of the dc-link current harmonics applying a double Fourier series is derived. The analytical results for the dc-link current spectra of continuous and discontinuous PWMs are presented and compared with measurement results taken from a converter test setup. A good match between theoretically expected and actually obtained experimental results can be stated. Moreover, characteristic differences between the investigated modulation strategies regarding their dc-link current spectra become evident.**

***Index Terms*—Capacitive energy storage, electrolytic capacitors, power conversion harmonics, pulsewidth-modulated (PWM) power converters.**

I. Introduction

NOWADAYS, pulsewidth-modulation (PWM) voltage-source converters constitute the most important means to control adjustable-speed drives or, generally, to serve as an active rectifier with low effects to the mains. An appropriate design of their power section has to be done, including the dc-link capacitor. The capacitor sizing basically aims at two issues: dc ripple voltage and, more importantly, capacitor lifetime, which can be linked directly to its power losses. These subjects are particularly affected by the capacitor currents, which coincide with the dc current harmonics in steady-state operation under certain presumptions. Thus, in general, the determination of such dc bus current harmonics facilitates the capacitor storage sizing of PWM-controlled power supplies as, for example, integrated in renewable energy applications [1], [2]. In the following paper, such an issue is specifically examined for a two-level three-phase PWM converter.

As for the measurement of harmonics in power electronics [3], there are also several sources on the calculation of the root-mean-square (rms) value of the dc-link ripple current in a two-level three-phase PWM converter [4]–[7], which eventually all lead to the same results regardless of the modulation strategy. This value is only affected by the duty cycles of the active space vectors, and thus, it will be of the same quantity for all modulation waveforms as long as only one converter is considered to be the source of harmonics on the dc bus. Another numerical approach is presented in [8], where the interference of two different PWM converters connected to the same dc bus is examined. There, it turns out that the phase shift of the respective pulse periods of each converter would have an effect on the dc bus ripple current. However, the amount of ripple current cannot be influenced by the modulation strategy in itself as applied only to a single converter, but the dispersion of the dc-link current spectra would be affected by the modulation strategy. Hence, the spectra have to be analyzed to predict, for instance, the resulting ripple voltage. As the dc-link capacitor constitutes an integral filter on the dc-link current, a change of the modulation strategy, and thus of the current spectra, introduces a change of the ripple voltage. This inherently can be seen in [5], where different modulation methods are analytically compared but only in the time domain. Regarding the aging of the capacitor, its heating and, thus, power losses are to be taken into account. These power losses are a function of the capacitor current and its series resistance. Usually, the rms value of the dc-link current is used for the design, but since the equivalent series resistance of a capacitor, i.e., $\mathrm{ESR}(\omega)$, shows some dependence on the frequency [9], [10], it is necessary to explicitly determine the capacitor current spectra to apply data sheet aging equations [11]. The dc current spectra have already been calculated and measured for sine triangular modulation in [6] and determined by an experiment for space vector modulation as well [9].

In the majority of the literature that deals with this issue, a constant dc current is assumed for analytical modulation as such models only focus on the power converter as a harmonic source in a first approach. This method is rather a benefit than a drawback as the results can either be considered as final outcomes for automotive purposes, for instance, or they can be utilized for further analysis as other dc current spectra can be superimposed by corresponding calculus. This would be the case for other converters being connected to the same dc bus, for example, where the same analysis could be applied with carrier phase shifts to be carefully treated.

This paper contributes a comprehensive analytical approach with the assumption of a constant dc-link current to explicitly determine the dc bus current spectra for any kind of modulation strategy, thereby utilizing the double Fourier series introduced in [14]. This approach has already been successfully applied

Manuscript received October 16, 2006; revised February 1, 2008. This work was supported by the government of Schleswig-Holstein, Germany.

M. H. Bierhoff was with the Christian-Albrechts University, 24098 Kiel, Germany. He is now with Still GmbH, 22113 Hamburg, Germany (e-mail: michael.bierhoff@still.de).

F. W. Fuchs is with the Institute for Power Electronics and Electrical Drives, Christian-Albrechts University, 24098 Kiel, Germany (e-mail: fwf@tf.uni-kiel.de).

Digital Object Identifier 10.1109/TIE.2008.921203

for the harmonics calculation of the three-phase currents of PWM voltage-source converters, as reported by various sources [15], [16]. In Section II, aging effects of capacitor ripple current and its spectral contents are explained to point out the basic motivation of this paper. Furthermore, in Section III, the principles of PWM are pointed out, which will be important for the analysis of Section IV, covering the derivation of the dc-link current average and rms value. The double Fourier series according to Black, as used for the determination of the dc bus harmonics, is introduced in Section V. Calculated results compared with experimental ones are presented in Section VI, revealing significant differences between the PWM methods, and then followed by a conclusion.

II. Capacitor Deterioration Due to Ripple

In [11], all failure modes of aluminum electrolytic capacitors are listed with the primary factors that influence the internal causes. Among the reasons for mishandled application are the following: mechanical stress, excessive thermal stress, excessive operating voltage, reverse voltage, excessive charge–discharge duty, and chloride contamination by assembly board cleaning. Apart from these physical quantities affecting capacitor aging, the ripple current is mentioned as a factor that again entails thermal stress as it directly affects the capacitor heating. Capacitor heating in itself causes electrolyte vaporization, which is followed by a capacitance drop and an increase of the ESR, respectively. A general formula for lifetime estimation is given in [11] with the expression

$$L_x = L_0 \cdot K_{\mathrm{Temp}} \cdot K_{\mathrm{Voltage}} \cdot K_{\mathrm{Ripple}} \tag{1}$$

where L_x is the capacitor lifetime to be estimated, L_0 is the base lifetime of the capacitor, and the other terms are acceleration terms with respect to the ambient temperature, voltage, and ripple current, respectively. In the following, analysis methods are developed for the determination of the last term, i.e., K_{Ripple}, as it contains spectral information regarding the capacitor current. Thus, an example for the determination of the factor K_{Ripple} that is applicable for the majority of the devices listed in [11] is given by

$$K_{\mathrm{Ripple}} = 2^{\left(1-\left(\frac{\sum^{n} I/f_n}{I_0 \cdot f_0}\right)^2\right)\cdot\frac{\Delta T_0}{5}}. \tag{2}$$

This equation applies for most of the cylindrical aluminum electrolytic capacitors, as offered in [11]. ΔT_0 represents the capacitor core temperature increase, whereas I_0 and f_0 denote the magnitude and frequency of the rated ripple current given by the data sheet, respectively. Accordingly, I_n and f_n denote the harmonic magnitudes and frequencies, respectively, as they actually appear within the capacitor current spectrum.

III. Principles of PWM

The basis for the analysis is a converter topology that is operated with PWM, as shown in Fig. 1. Fig. 2 depicts the corresponding pulse train for switches V_1, V_3, and V_5 during an exemplary switching period. Taking only these switches into consideration is sufficient since only the switched currents i_{V1}, i_{V3}, and i_{V5} will be regarded for the derivations. For this example, the instantaneous voltage command space vector is located in the first sector of the vector space that is spanned by the six possible switching states of the active space vectors.

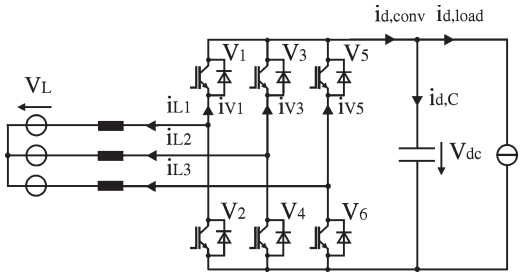

Fig. 1. Three-phase voltage-source converter topology.

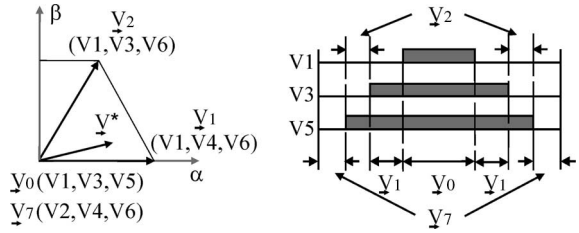

Fig. 2. Switching scheme for upper bridge valves in the first sector of the complex plane.

It is well known that the command space vector is approximated by a sliding mean value of the switched space vectors $\underline{V}_1$, $\underline{V}_2$, and $\underline{V}_0$, and $\underline{V}_7$ being turned on for the time periods t_1, t_2, t_0, and t_7, respectively, during the PWM pulse period T_p [12], [13]. These space vectors, in turn, are achieved by a corresponding switching combination of the six semiconductor switches (see Fig. 2). During the time period t_0, all upper switches (Fig. 1) are turned on, whereas during t_7, only the lower ones are turned on. The given proportions of switching intervals for the respective switches, as shown in Fig. 2, are only valid for the sector that the command vector $\underline{V}^*$ resides in according to Fig. 2. Nevertheless, examination of this scope of the complex vector plain is sufficient for the following calculations, as will be seen further on.

In [16]–[18], the direct relation between space vector and naturally sampled carrier PWM is explained. From these relations, it can be concluded that the carrier function that would be applied according to Fig. 2 is a triangular function, which can be deduced from the symmetrical arrangement of switching duty cycles. Moreover, with this analogy, the PWM pulse period T_p would be equal to the carrier period for the comparable carrier-based PWM. It should be pointed out that the direction of the power flow does not affect the calculation of dc-link current harmonics, as presented here. Thus, the ac and dc loads can be arbitrarily chosen, either passive or active.

IV. DC-Link Current Average and RMS Value

A. Construction of the DC Current Trajectory

When compared to Fig. 1, it becomes evident from Fig. 2 that only the time periods t_1 and t_2, which are equivalent to

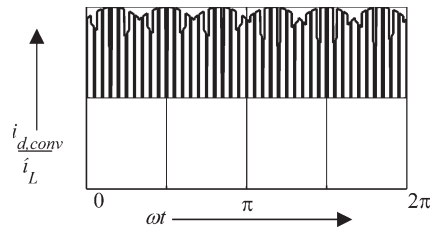

Fig. 3. DC current trajectory at modulation index $M = 1$, phase shift $\varphi = 0$, and pulse ratio $p = 20$.

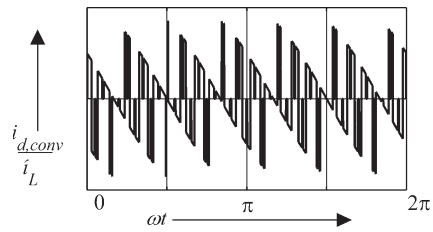

Fig. 4. DC current trajectory at modulation index $M = 1$, phase shift $\varphi = 90°$, and pulse ratio $p = 20$.

the duty cycles of the active space vectors, contribute to a current flow into the dc bus. During the other two time periods t_0 and t_7, either the upper half bridge or the lower one is short circuited, and the dc bus is free of any current. Thus, these time spans constitute the zero duty cycles. According to [16]–[18], different modulation waveforms can be distinguished by the proportion of these zero voltage time periods t_0 and t_7, whereas the sum of both only depends on the modulation index M and not on the modulation waveform. Therefore, there are no effects of the modulation waveform on the dc current ripple.

Even a different distribution of the active space vector cycles, as would be the case for different carrier waveforms, does not affect the dc current ripple; however, there are effects on the spectra distribution.

Figs. 3 and 4 show exemplary dc current outlines in the time domain as they would occur for common space vector modulation at a modulation index of $M = 1$ with a phase shift between the fundamental ac voltage and current at the converter terminals of $\varphi = 0$ (Fig. 3) and $\varphi = 90°$ (Fig. 4). The time scope that is revealed corresponds to one fundamental period of the ac voltage. The pulse ratio of $p = 20$ would result in a carrier frequency of 1 kHz if a fundamental frequency of 50 Hz was assumed.

In Fig. 3, it can be seen that the dc current mean value, and thus the transferred active power, can only be increased by a higher modulation index. Fig. 4 shows an operating point where the mean value of the dc bus current and the transferred active power are both equal to zero.

B. Calculation of the DC Current Components

With appropriate simplifications such as steady-state considerations and the assumption of sinusoidal trajectories for the three-phase line currents, the dc-link current harmonics can be determined irrespective of the power flow direction. Another simplification that is usually introduced is the dc load current $i_{d,\mathrm{load}}$, which is considered a constant dc value [4]–[6] as is assumed here. If additionally a fairly high switching frequency is assumed, the average value of the dc bus current $\bar{i}_{d,\mathrm{conv}}$ can be determined by (3) [4], where ω indicates the fundamental angular frequency. The standardized time periods t_1/T_p and t_2/T_p can be determined by (4) and (5). Thus

$$\bar{i}_{d,\mathrm{conv}} = \frac{3}{\pi \cdot T_p} \cdot \int_0^{\pi/3} (i_{L1}(\omega t) \cdot t_1(\omega t) - i_{L3}(\omega t) \cdot t_2(\omega t)) \cdot d\omega t \tag{3}$$

$$\frac{t_1}{T_p} = \frac{\sqrt{3}}{2} \cdot M \cdot \sin\left(\frac{\pi}{3} - \omega t\right) \tag{4}$$

$$\frac{t_2}{T_p} = \frac{\sqrt{3}}{2} \cdot M \cdot \sin(\omega t). \tag{5}$$

Obviously, these expressions are independent of the modulation or carrier waveform. With a periodic behavior for each sector with a radial extension of $\pi/3$, the mean value calculation, as any of the following rms value calculation, can be confined to an angle of $\pi/3$. Thus, only one sector of a range of $\pi/3$ needs to be regarded in the calculations. When the expressions for the switching period of active space vectors $t_1(\omega t)$ and $t_2(\omega t)$ are substituted by (4) and (5) in (3), it yields the simple expression (6) for the mean value of the dc bus current $\bar{i}_{d,\mathrm{conv}}$ (see also [4]–[6]). On the other hand, it is obvious that the rms value of the dc bus current $\tilde{i}_{d,\mathrm{conv}}$ can be determined in an analog manner to that of the average value (7). The rms value of the capacitor current $\tilde{i}_{d,C}$ can now be found by the geometrical difference of the complete rms of the dc current value (7) minus the corresponding mean value (6), which results in (8), as already stated in [4]–[6]. This result, obviously, is a function of the modulation index M and phase shift angle φ. Note that all equations specified in this section only stay valid as long as the command voltage space vector resides in the first sector of the complex vector space. For the other sectors, similar expressions could be found, eventually rendering the same results. Therefore

$$\bar{i}_{d,\mathrm{conv}} = \frac{3}{4} \cdot \hat{i}_L \cdot M \cdot \cos(\varphi) \tag{6}$$

$$\tilde{i}_{d,\mathrm{conv}} = \sqrt{\frac{3}{\pi \cdot T_p} \cdot \int_0^{\pi/3} (i_{L1}^2(\omega t) \cdot t_1(\omega t) + i_{L3}(\omega t)^2 \cdot t_2(\omega t)) \cdot d\omega t}$$

$$\tilde{i}_{d,\mathrm{conv}} = \sqrt{\frac{\sqrt{3}}{\pi} \cdot M \cdot \hat{i}_L^2 \cdot \left(\frac{1}{4} + \cos^2(\varphi)\right)} \tag{7}$$

$$\tilde{i}_{d,C} = \hat{i}_L \cdot \sqrt{M \left(\frac{\sqrt{3}}{4\pi} + \cos^2(\varphi) \cdot \left(\frac{\sqrt{3}}{\pi} - \frac{9M}{16}\right)\right)}. \tag{8}$$

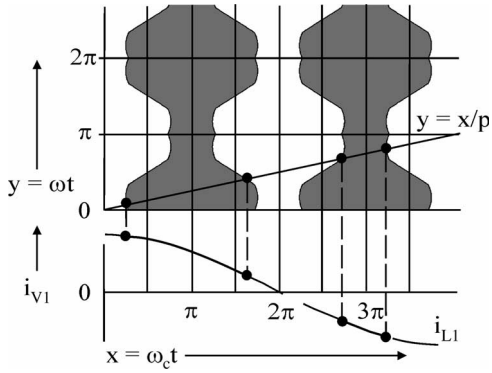

Fig. 5. Geometric wall model as applied on a modulation function corresponding to space vector modulation with equal weighting of zero space vectors and a triangular carrier.

V. DC-Link Current Spectra Described by a Double Fourier Series

A. Geometric Wall Model According to Black

A viable but tedious approach to analytically determine the dc-link current spectra is given in [6]. Another one utilizing the geometric wall model [14], resulting in a double Fourier series, is presented here. This method provides a fairly simple way to obtain expressions for the Fourier coefficients of line-side or dc-side current harmonics generated by any conventional modulation strategy.

Initially, the geometric wall model was applied for the analysis of asynchronous sinusoidal modulation schemes to overcome the problems caused by the nonperiodic behavior of the pulse waveform [15]. A plain view for the actually considered 3-D model is given in Fig. 5. The "walls" are represented by the boundaries of the shaded areas, representing the actually applied modulation waveform. These areas are arranged in a symmetrical manner, always according to the corresponding carrier signal. Originally considering the ac voltage spectra, the third dimension of this model is introduced by determining the height of these areas (walls) to the dc-link voltage $V_{\rm dc}$ [15], [16]. In the case of a current-source converter, it would be the dc-link current, as stated in [19]. The important modification to apply this method on the dc current is to adjust the height of the walls to the instantaneous value of $i_L(\omega t)$. The walls are oriented perpendicular to the $x-y$ plane, where y represents the fundamental angle ωt, and x is equivalent to the increasing angle of carrier periods $\omega_c t$. The assumption of unipolar switching introduces an erroneous dc component when the ac voltage harmonics are regarded [15]. However, since the resulting pulsewidths directly agree with the switch duty cycles t_n/T_p, this model is a perfect match of the pulse train, as given in Fig. 2. Moreover, in this case, it is valid for the entire region of one fundamental period. The intersections of the straight line $f(y) = x/p$ with the modulation waveforms $x = \pi/2\ ((2n+1)3\cos(\omega t))$ indicate a pulse transition of $i_L(\omega t)$. Here, p is the carrier ratio $(p = \omega_c/\omega)$, ω_c is the carrier angular frequency, and ω is the fundamental angular frequency. An illustration of this method is given in Fig. 5 with a modulation waveform corresponding to the commonly used space vector modulation with equal weighting of zero space vectors along with natural sampling. The modulation waveforms are symmetrically arranged around lines of multiples of π to realize a model that supports a triangular carrier wave shape. As the widths of the resulting pulses are equal to the switching duty cycles of one semiconductor switch and the instantaneous value of the corresponding phase current is assigned to their height, these pulses consequently resemble the outline of one of the switch currents i_{V1}, i_{V3}, and i_{V5}. This includes the corresponding freewheeling diodes. These currents solely differ from each other by the phase shift of the respective modulation function and phase current. Evidently, the sum of all instantaneous valve currents $i_{V1} + i_{V3} + i_{V5}$ would finally deliver the instantaneous dc bus current value $i_{d,\rm conv}$.

It should be remarked that by this method, even the influence of any other PWM inverter that is connected to the dc bus can be taken into account by simply adding its current portions to the foregoing sum.

B. Evolution of the Double Fourier Series

As the wall pattern is periodic in 2π for both axes, the pulse function $F(x, y)$ may be expressed as a double Fourier series (9), where the complex Fourier coefficients can be determined with the double integral (10) [14]–[16]. Thus

$$\begin{aligned} F(x,y) = {} & \frac{A_{00}}{2} + \sum_{n=1}^{\infty} [A_{0n}\cos(ny) + B_{0n}\sin(ny)] \\ & + \sum_{m=1}^{\infty} [A_{m0}\cos(mx) + B_{m0}\sin(mx)] \\ & + \sum_{m=1}^{\infty}\sum_{n=\pm 1}^{\pm\infty} [A_{mn}\cos(mx+ny) \\ & \qquad + B_{mn}\sin(mx+ny)] \end{aligned} \tag{9}$$

$$\begin{aligned} C_{mn} &= A_{mn} + jB_{mn} \\ &= \frac{1}{2\pi^2}\int_0^{2\pi}\int_0^{2\pi} F(x,y)\cdot e^{j(mx+ny)}dx\,dy. \end{aligned} \tag{10}$$

Here, it can be seen that, in particular, the expression of complex Fourier coefficients seems to result in a compact equation. To apply this general equation for the calculation of actual pulsed converter quantity spectra, the function $F(x, y)$ has to be properly determined. In Fig. 5, the function $F(x, y)$ is resembled by the height of the walls at the point of cross section with the function $f(y) = x/p$. Thus, in the case of ac voltage spectral analysis, the function $F(x, y)$ would be the intermittent dc bus voltage. In the case of valve current spectral analysis, it is the interrupted line current. With a quasi-continuous interpretation of the problem, the interrupts of the original continuous functions can be accounted for by the introduction of appropriate boundaries for the inner integral term, which coincide with intersections of the function x/p with the shaded areas of Fig. 5. Thus, these areas, which contain the modulation waveforms $M(y)$ incorporating a certain offset, constitute the boundaries of the inner integral term as functions of $yf(y)$. The actual application of these findings is presented in the next section.

C. Derivation of DC-Link and Capacitor Current Harmonics

For all upcoming calculus, natural sampling is assumed, which is similar to regular sampling as long as a sufficiently high carrier ratio p is assumed. Furthermore, only a high carrier ratio ($p > 20$) will satisfy the claim that carrier sideband interference can be neglected. If employed for the example of naturally sampled modulation with a triangular carrier, as shown in Fig. 5, the actual complex Fourier coefficients of the switch current ${}^{mn}i_{V1}$ would be identified by (11), whereas a modulation waveform combined with a sawtooth carrier with a trailing edge requires a term such as (12). Therefore

$${}^{mn}i_{V1} = \frac{\hat{i}_L}{2\pi^2} \int_0^{2\pi} \left(\int_{\frac{\pi}{2}(1-M(y))}^{\frac{\pi}{2}(3+M(y))} \cos(y-\varphi) \cdot e^{j(mx+ny)} dx \right) dy \tag{11}$$

$${}^{mn}i_{V1} = \frac{\hat{i}_L}{2\pi^2} \int_0^{2\pi} \left(\int_0^{\pi(1+M(y))} \cos(y-\varphi) \cdot e^{j(mx+ny)} dx \right) dy. \tag{12}$$

Equations (13)–(15) render the modulation waveforms for the three most common PWM strategies, as discussed here. The most simple modulation function, which is the cosine function (13), will be designated as Mod 1 from now on. The modulation function that is constituted by the well-known space vector PWM with equal utilization of zero space vectors (14) should be denoted as Mod 2. The representative discontinuous modulation function that has been investigated here is given by (15) and will be related to as Mod 3 in the following discussion. It would cause the least switching losses at a power factor of unity. Hence, it can be considered somewhat comparable to the other modulation functions as long as a phase shift of $\varphi = 0$ is considered. To preserve clarity, the modulation waveforms Mod 1 to Mod 3 are depicted in Fig. 6 as they appear over one fundamental period. Thus

$$M(\omega t) = M \cdot \cos(\omega t) \tag{13}$$

$$M(\omega t) = \begin{cases} \frac{\sqrt{3}}{2} \cdot M \cdot \cos\left(\omega t - \frac{\pi}{6}\right), & \text{for } 0 < \omega t < \frac{\pi}{3} \\ & \text{or } \pi < \omega t < \frac{4\pi}{3} \\ \frac{3}{2} \cdot M \cdot \cos(\omega t), & \text{for } \frac{\pi}{3} < \omega t < \frac{2\pi}{3} \\ & \text{or } \frac{4\pi}{3} < \omega t < \frac{5\pi}{3} \\ \frac{\sqrt{3}}{2} \cdot M \cdot \cos\left(\omega t + \frac{\pi}{6}\right), & \text{for } \frac{2\pi}{3} < \omega t < \pi \\ & \text{or } \frac{5\pi}{3} < \omega t < 2\pi \end{cases} \tag{14}$$

$$M(\omega t) = \begin{cases} 1, & \text{for } -\frac{\pi}{6} < \omega t < \frac{\pi}{6} \\ \sqrt{3} \cdot M \cdot \cos\left(\omega t - \frac{\pi}{6}\right) - 1, & \text{for } \frac{\pi}{6} < \omega t < \frac{\pi}{2} \\ \sqrt{3} \cdot M \cdot \cos\left(\omega t + \frac{\pi}{6}\right) + 1, & \text{for } \frac{\pi}{2} < \omega t < \frac{5\pi}{6} \\ -1, & \text{for } \frac{5\pi}{6} < \omega t < \frac{7\pi}{6} \\ \sqrt{3} \cdot M \cdot \cos\left(\omega t - \frac{\pi}{6}\right) + 1, & \text{for } \frac{7\pi}{6} < \omega t < \frac{3\pi}{2} \\ \sqrt{3} \cdot M \cdot \cos\left(\omega t + \frac{\pi}{6}\right) - 1, & \text{for } \frac{3\pi}{2} < \omega t < \frac{11\pi}{6}. \end{cases} \tag{15}$$

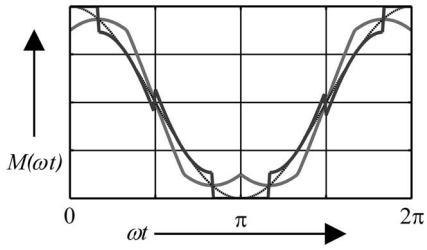

Fig. 6. Modulation waveforms Mod 1 (black dotted), Mod 2 (space vector with equal zero space vector utilization, light gray), and Mod 3 (discontinuous modulation waveform, dark gray) at a modulation index of $M = 1$ each.

Obviously, only the boundaries of the inner integral term of (11) and (12) are affected by the choice of different modulation strategies. Hence, the Fourier coefficients of the switch current ${}^{mn}i_V$ caused by any other modulation waveform can be accordingly determined. The results of these expressions can be interpreted as follows: The index m indicates the mth carrier frequency band, whereas the index n marks the nth multiple of the fundamental frequency starting with $m \geq 0$ and with $n = -\infty, \ldots, +\infty$ from each multiple of the carrier frequency on. Here, the magnitude of the index n is confined to half the carrier ratio unless sideband interference is accounted for. Equation (11) has been exemplarily dissolved for the most simple case, i.e., a cosine modulation function (see the Appendix). It can be solved for the other modulation waveforms, as well by applying the appropriate identities given in [16]. Therefore

$${}^{mn}i_{d,C} = {}^{mn}i_{V1} + {}^{mn}i_{V3} + {}^{mn}i_{V5}. \tag{16}$$

As already mentioned, the dc bus current is the result of superposition of all three switch currents in the upper part of the bridge. Hence, the Fourier coefficients of the dc-link current are the sum of all complex Fourier coefficients describing the valve currents in the upper bridge (16).

VI. Calculation and Measurement Results of DC-Link Current Harmonics

A. Analytical Results

Calculations of the dc-link harmonics were carried out by means of the double Fourier series for all three modulation strategies along with a triangular waveform each. The derived formulas have been evaluated with Mathcad. The phase shift between voltage and current fundamentals at the converter terminals was set to $\varphi = 5^\circ$ for all calculations for comparable conditions regarding the measurements. A carrier ratio of $p = 60$ was assumed, and the sideband sequences were confined to 40 elements each. It should be pointed out that all spectra of discontinuous modulation waveforms look somewhat similar. However, the one treated here ensures minimum switching losses for the presumed power factor [16].

The outcomes are presented in the diagrams of Figs. 7–9, where the peak values of the capacitor current harmonics ${}^{\nu}\hat{i}_{d,C}$ are standardized with the peak value of the ac current fundamental ${}^{1}\hat{i}_L$, and the frequency f is scaled by multiples of the carrier frequency f_c. The spectra were plotted at discrete values

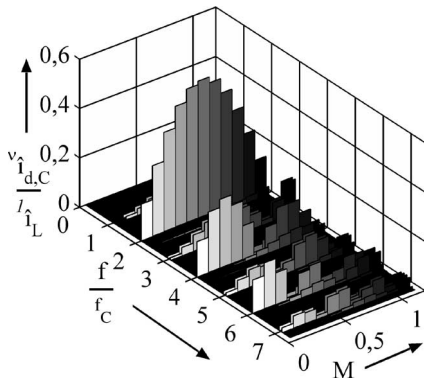

Fig. 7. Calculated dc-link current spectra for Mod 1 (cosine modulation waveform) combined with a triangular carrier function ($\varphi = 5°$).

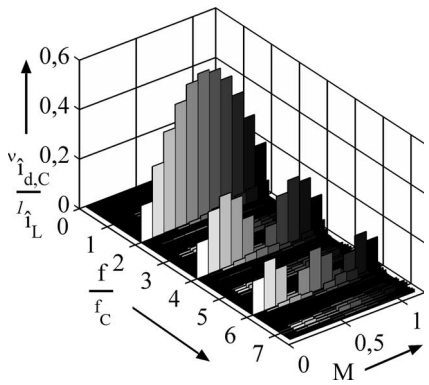

Fig. 8. Calculated dc-link current spectra for Mod 2 (space vector modulation with equal utilization of zero space vectors) combined with a triangular carrier function ($\varphi = 5°$).

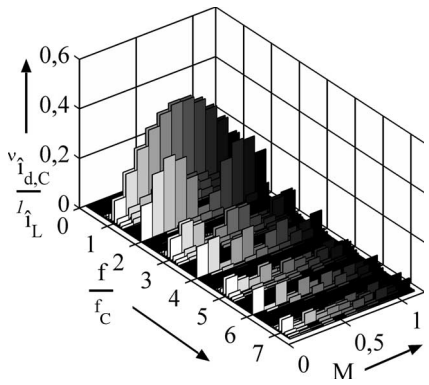

Fig. 9. Calculated dc-link current spectra for Mod 3 (discontinuous modulation waveform) combined with a triangular carrier function ($\varphi = 5°$).

of the modulation index ($M = 0.1, 0.2, \ldots, 1.1$). Comparing the harmonic performance of the different modulation functions, it is striking that for the discontinuous one, Mod 3, even when a triangular carrier is applied to the first carrier frequency band, is still occupied by a significant bunch of spectral lines. This also applies for the cosine modulation function in an alleviated manner as the modulation index increases. Thus, the modulation method Mod 2 seems to be favorable in terms of dc-link voltage harmonics reduction, as already stated in [5].

TABLE I
PARAMETERS OF THE EXPERIMENTAL TEST SETUP

Quantity	Value
Rated power of converter, P_N	22 kW
DC link voltage, V_{DC}	560 V
Fundamental frequency, f	50 Hz
Carrier frequency, f_c	3 kHz
AC load resistance, R_L	15 Ω
AC load inductance, L_F	4.5 mH
Fundamental phase shift φ	5.4°

B. Measurement Results

Measurements were taken from a voltage-source converter, as depicted in Fig. 1, with a rated power of 22 kW and operated with a dc-link voltage of $V_{\rm dc} = 560$ V. A passive three-phase ac load of $R_L = 15\ \Omega$ in series with a filter inductance of $L_F = 4.5$ mH was installed at the ac side, which causes a phase shift of $\varphi = 5.4°$ at an applied fundamental frequency of $f = 50$ Hz. Thus, it yields a fundamental power factor at the converter terminals $\cos(\varphi)$ of almost unity. The switching (carrier) frequency f_c was set to $f_c = 3$ kHz. Refer to Table I for the parameters in brief. Compliant to the analytical considerations, the dc bus was fed by a diode bridge to deliver a well-smoothed dc load current $i_{d,\rm load}$. The dc bus current was measured for steady-state operation by a current probe. The current measurements were sampled and plotted with an ONO SOKKI CF-5210 FFT analyzer. The data evaluation, including the Fourier analysis, was done using MATLAB.

Once again, the modulation waveforms revealed in Fig. 6 were compared along with a triangular carrier wave shape each. Figs. 10–12 show the measured counterparts of the calculated spectra in Figs. 7–9, which correspond quite well. As already predicted by the theoretical analysis, it can be seen that PWM method Mod 3 exhibits the worst harmonic behavior as the majority of spectral lines lies below that of the other modulation waveforms. Hence, the advantage of less switching losses for PWM method Mod 3, as compared to the other ones, always has to be considered in association with the weaker harmonic performance.

Resulting deviations originate from inaccuracies of the measurements and, in particular, from inexact approximations that have been assumed for the calculations. The ac-line current does not possess an exact pure sinusoidal trajectory, which exhibits the most significant impact on results gained at low modulation indexes. Moreover, a minor error occurs by the assumption of natural sampling instead of actually regular-sampled PWM, which can be overcome by little modification of the presented calculation methods [16]. The apparent differences between Figs. 9 and 12 can be explained by the low number of Fourier coefficients that are regarded in the calculation of harmonics at multiples of the carrier frequency ($n = 20$). In contrast to the other modulation waveforms, this

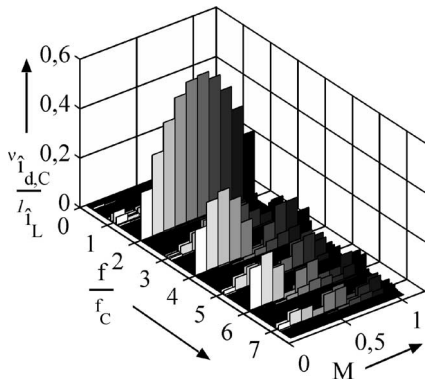

Fig. 10. Measured dc-link current spectra for Mod 1 (cosine modulation waveform) combined with a triangular carrier function ($\varphi = 5°$).

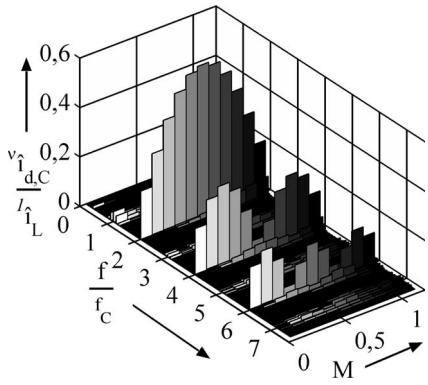

Fig. 11. Measured dc-link current spectra for Mod 2 (space vector modulation with equal utilization of zero space vectors) combined with a triangular carrier function ($\varphi = 5°$).

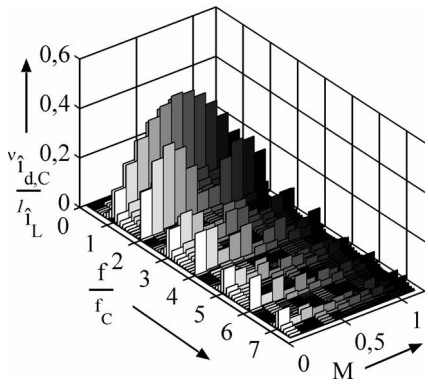

Fig. 12. Measured dc-link current spectra for Mod 3 (discontinuous modulation waveform) combined with a triangular carrier function ($\varphi = 5°$).

is not sufficient for the last modulation waveform to achieve similar accuracy of the calculated sidebands.

VII. Conclusion

A new method for the calculation of dc-link current harmonics for voltage-source converters operated by any modulation strategy is presented. As means of analysis, the geometric wall model approach for the determination of a double Fourier series describing the dc current harmonics is proposed and applied to three selected cases. With this method, it is feasible to analytically determine the dc bus current spectra for all kinds of modulation strategies. Moreover, it gives the opportunity to account for any other converter that is connected to the same dc bus as long as the phase shift of the resulting harmonics is carefully regarded.

Hence, an extension of the presented approach for converters (inverters, as well as active rectifiers) arbitrarily additionally connected to the same dc bus can be conducted by applying the same analytical rules for those converters, as presented here. A geometric addition of all such determined complex spectra would result in the total harmonic load of the corresponding capacitors if the relative phase shift of carrier signals is known. This always had to be done for each particular operating point to be considered, where, in the case of inverters, the fundamental frequency of the corresponding ac currents would be an additional parameter—in addition to amplitude and phase shift—to be considered.

The analytical results render information on the predominant influence of the modulation strategy on the dc bus current spectra dispersion. Different exemplary modulation functions are investigated, i.e., continuous and discontinuous ones along with a triangular carrier each. The theoretical outcomes were proved by additional measurements. It is evident that the presented method contributes to dc bus capacitor sizing as it facilitates the prediction of the dc-bus current spectra for any kind of conventional modulation method with a fixed pulse frequency.

Appendix

As an example, we present the dissolution of (11) for a cosine modulation waveform (13). As such, (11) can also be written as (18) with (17), i.e.,

$$\cos(\alpha) = \frac{1}{2} \cdot (e^{j\alpha} + e^{-j\alpha}) \tag{17}$$

$$\begin{aligned} {}^{mn}i_{V1} = {} & \frac{\hat{i}_L}{j4\pi^2 m} \\ & \times \left[e^{j\left(m \cdot \frac{3\pi}{2} - \varphi\right)} \int_0^{2\pi} e^{j(n+1)y} \cdot e^{j\left(m \cdot \frac{\pi}{2} \cdot M \cdot \cos(y)\right)} dy \right. \\ & - e^{j\left(m \cdot \frac{\pi}{2} - \varphi\right)} \int_0^{2\pi} e^{j(n+1)y} \cdot e^{j\left(-m \cdot \frac{\pi}{2} \cdot M \cdot \cos(y)\right)} dy \\ & + e^{j\left(m \cdot \frac{3\pi}{2} + \varphi\right)} \int_0^{2\pi} e^{j(n-1)y} \cdot e^{j\left(m \cdot \frac{\pi}{2} \cdot M \cdot \cos(y)\right)} dy \\ & \left. - e^{j\left(m \cdot \frac{\pi}{2} + \varphi\right)} \int_0^{2\pi} e^{j(n-1)y} \cdot e^{j\left(-m \cdot \frac{\pi}{2} \cdot M \cdot \cos(y)\right)} dy \right]. \end{aligned} \tag{18}$$

With the identity given by (19) (see also [14]), (18) can be turned into (20), which comprises Bessel functions of the first kind and the nth order, i.e.,

$$J_n(Z) = \frac{j^{-n}}{2\pi} \cdot \int_0^{2\pi} e^{jZ \cdot \cos(\alpha)} e^{jn \cdot \alpha} d\alpha \tag{19}$$

$$
\begin{aligned}
{}^{mn}i_{V1} = \frac{\hat{i}_L \cdot j^n}{2\pi \cdot m} \Bigg[& e^{j\left(m\cdot\frac{3\pi}{2}-\varphi\right)} \cdot J_{n+1}\left(m\frac{\pi}{2}\cdot M\right) \\
& - e^{j\left(m\cdot\frac{\pi}{2}-\varphi\right)} \cdot J_{n+1}\left(-m\frac{\pi}{2}\cdot M\right) \\
& + e^{j\left(m\cdot\frac{3\pi}{2}+\varphi\right)} \cdot J_{n-1}\left(m\frac{\pi}{2}\cdot M\right) \\
& - e^{j\left(m\cdot\frac{\pi}{2}+\varphi\right)} \cdot J_{n-1}\left(-m\frac{\pi}{2}\cdot M\right) \Bigg]
\end{aligned} \tag{20}
$$

for $n = -\infty, \ldots, +\infty$ and $m = 1, 2, \ldots$.

As can be seen, the case for $m = 0$ cannot be regarded by (20). Thus, a distinction of cases yields (21), as deduced from (9), i.e.,

$$
{}^{0n}i_{V1} = \frac{\hat{i}_L}{j2\pi^2} \int_0^{2\pi} e^{jn\cdot y}\left(\pi + \pi \cdot M \cdot \cos(y)\right) \cdot \cos(y-\varphi) dy. \tag{21}
$$

It turns out that after employing l'Hospital's rule on (21), there are only values remaining for $n = 0$, 1, 2, as can be seen by

$$
{}^{0n}i_{V1} = \begin{cases} \frac{M\cdot\hat{i}_L}{j\cdot 2} \cdot \cos(\varphi), & \text{if } n = 0 \\ \frac{\hat{i}_L}{j\cdot 2} \cdot e^{j\varphi}, & \text{if } n = 1 \\ \frac{M\cdot\hat{i}_L}{j\cdot 4} \cdot e^{j\varphi}, & \text{if } n = 2. \end{cases} \tag{22}
$$

This is the most simple but as such the best example for the dissolution of the double integrals. The modulation waveforms (14) and (15) are described by either constant elements or cosine expressions, where the argument is always specified by the fundamental angular frequency. Thus, the dissolution of the corresponding integral expressions for each section of case distinction would render similar expressions as follows for only a cosine modulation waveform.

REFERENCES

[1] M. Ortuzar, J. Moreno, and J. Dixon, "Ultracapacitor-based auxiliary energy system for an electric vehicle," *IEEE Trans. Ind. Electron.*, vol. 54, no. 4, pp. 2147–2156, Aug. 2007.

[2] J.-M. Kwon, K.-H. Nam, and B.-H. Kwon, "Photovoltaic power conditioning system with line connection," *IEEE Trans. Ind. Electron.*, vol. 53, no. 4, pp. 1048–1054, Jun. 2006.

[3] V. A. Katic, J. M. Knezevic, and D. Graovac, "Application-oriented comparison of the methods for AC/DC converter harmonics analysis," *IEEE Trans. Ind. Electron.*, vol. 50, no. 6, pp. 1100–1108, Dec. 2003.

[4] J. W. Kolar, H. Ertl, and F. C. Zach, "Calculation of the passive and active component stress of three phase PWM converter systems with high pulse rate," in *Proc. 3rd Eur. Conf. Power Electron. Appl.*, Aachen, Germany, 1989, vol. 3, pp. 1303–1311.

[5] P. A. Dahono, Y. Sato, and T. Kataoka, "Analysis and minimization of Ripple components of input current and voltage of PWM inverters," *IEEE Trans. Ind. Appl.*, vol. 32, no. 4, pp. 945–950, Jul./Aug. 1996.

[6] F. Renken, "Analytic calculation of the DC-link capacitor current for pulsed three phase inverters," in *Proc. 11th Int. Conf. Power Electron. Motion Control*, Riga, Latvia, 2004. CD ROM.

[7] M. Winkelnkemper, "Reduzierung von Zwischenkreiskapazitäten in Frequenzumrichtern für Niederspannungsantriebe," Ph.D. dissertation, TU Berlin, Berlin, Germany, 2005.

[8] M. Winkelnkemper and S. Bernet, "Design and optimization of the DC-link capacitor of PWM voltage source inverter with active frontend for low-voltage drives," in *Proc. 10th Eur. Conf. Power Electron. Appl.*, Toulouse, France, 2003. CD ROM.

[9] F. D. Kieferndorf, M. Förster, and T. A. Lipo, "Reduction of DC bus capacitor ripple current with PAM/PWM converter," in *Proc. 10th Eur. Conf. Power Electron. Appl.*, Toulouse, France, 2003. CD ROM.

[10] M. L. Gasperi, "A method for predicting the expected life of bus capacitors," in *Conf. Rec. IEEE IAS Annu. Meeting*, 1997, vol. 2, pp. 1042–1047.

[11] Nippon Chemi—Con., *Aluminum Electrolytic Capacitors 2005/2006*, pp. 43–45, 2005. Application handbook.

[12] S. R. Bowes and D. Holliday, "Optimal regular sampled PWM inverter control techniques," *IEEE Trans. Ind. Electron.*, vol. 54, no. 3, pp. 1547–1559, Jun. 2007.

[13] A. Cataliotti, F. Genduso, A. Raciti, and G. R. Galluzzo, "Generalized PWM-VSI control algorithm based on a universal duty cycle expression: Theoretical analysis, simulation results and experimental validations," *IEEE Trans. Ind. Electron.*, vol. 54, no. 3, pp. 1569–1580, Jun. 2007.

[14] H. S. Black, *Modulation Theory*. New York: Van Nostrand, 1953.

[15] J. F. Moynihan, M. G. Egan, and J. M. D. Murphy, "Theoretical spectra of space-vector-modulated waveforms," *Proc. Inst. Electr. Eng.—Electric Power Applications*, vol. 145, no. 1, pp. 17–24, Jan. 1998.

[16] D. G. Holmes, T. A. Lipo, *Pulse Width Modulation for Power Converters*, IEEE press series on power engineering. Piscataway, NJ: IEEE Press, 2003.

[17] K. Zhou and D. Wang, "Relationship between space-vector modulation and three-phase carrier based PWM: A comprehensive analysis," *IEEE Trans. Ind. Electron.*, vol. 49, no. 1, pp. 186–196, Feb. 2002.

[18] F. Jenni and D. Wüest, *Steuerverfahren für Selbstgeführte Stromrichter*. Stuttgart, Germany: B.G. Teubner, 1995.

[19] M. Bierhoff, F. W. Fuchs, and S. Pischke, "Theoretical output current spectra of three phase current source converters," in *Proc. 11th Eur. Conf. Power Electron. Appl.*, Dresden, Germany, 2003. CD ROM.

Michael H. Bierhoff was born in Dortmund, Germany, in 1974. He received the Dipl.-Ing. (FH) degree from the University of Applied Science, Dortmund, Germany, in 2001 and the Ph.D. degree from the Christian Albrechts University, Kiel, Germany.

Since 2006, he has been with Still GmbH, Hamburg, Germany, as a Research Engineer. His fields of interest include power loss estimation, harmonic determination, and control of PWM power electronics converters.

Mr. Bierhoff is a member of the Association of German Electrical and Electronics Engineers (VDE).

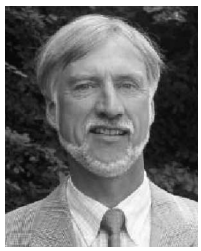

Friedrich Wilhelm Fuchs (M'97–SM'01) was born in Minden, Germany, in 1948. He received the Dipl.-Ing. and Ph.D. degrees from the RWTH University of Technology Aachen, Aachen, Germany, in 1975 and 1982, respectively.

In 1975, he carried out research work at the University in Aachen, mainly on ac drives for battery-powered electric vehicles. Between 1982 and 1996, he was a Group Manager in the field of power electronics and electrical drives in a medium-sized company. In 1991, he joined the Converter Division, AEG, Berlin, Germany, where he was the Managing Director for research, design, and development of the complete range of drive products, drive systems, and high-power supplies from 5 kVA to 50 MVA. In 1996, he joined the newly founded Faculty of Engineering, Christian-Albrechts University, Kiel, Germany, as a Full Professor, being the Head of and building up the Institute for Power Electronics and Electrical Drives, which is a member of the Wind Energy Competence Centre (CEwind), Schleswig-Holstein, Germany. The interests of this team are power semiconductor application and their control, as well as variable-speed drives with focus on modern control, diagnosis, and fault-tolerant drives with special regard to renewable energy systems, particularly wind energy. He has authored or coauthored more than 70 papers.

Dr. Fuchs is a member of the Association of German Electrical and Electronics Engineers (VDE) and the European Power Electronics and Drives Association. He is a convener and an international speaker of the German standardization committee K331 (TC22) for power electronics.